

Article

Stator Curvature Optimization and Analysis of Axial Hydraulic Vane Pumps

Yongguo Sun *, Dong Xue, Shisheng Liu, Jinghang Wu and Xingyu Bai

School of Mechanical Power Engineering, Harbin University of Science and Technology, Harbin 150008, China

* Correspondence: sygedu@163.com; Tel.: +86-153-0480-5959

Abstract: Aiming at the problem of large vibration of a high-subside stator inner cavity curve vane pump, the force analysis of the vane at the transition curve is carried out, and the functional relationship between the vane turning angle θ , the large arc radius R , the small arc radius r and the sliding friction is established. The particle swarm algorithm is used to optimize the solution of the objective function, and the optimized parameter values are brought into the MATLAB simulation program to obtain the optimized stator curve profile diagram. The dynamic performance of the vane pump before and after optimization is simulated using ADAMS. The results show that: the acceleration of the vane pump slide is significantly reduced; the friction between the slide and the slide groove is significantly reduced; the contact force between the slide and the stator is significantly reduced; the impact vibration of the optimized vane pump is significantly reduced; and the dynamic performance of the vane pump is improved.

Keywords: stator; blade force analysis; algorithm optimization; dynamic performance



Citation: Sun, Y.; Xue, D.; Liu, S.; Wu, J.; Bai, X. Stator Curvature Optimization and Analysis of Axial Hydraulic Vane Pumps. *Energies* **2022**, *15*, 6229. <https://doi.org/10.3390/en15176229>

Academic Editors: Firoz Alam and Xiaolin Wang

Received: 30 July 2022

Accepted: 22 August 2022

Published: 26 August 2022

Publisher's Note: MDPI stays neutral with regard to jurisdictional claims in published maps and institutional affiliations.



Copyright: © 2022 by the authors. Licensee MDPI, Basel, Switzerland. This article is an open access article distributed under the terms and conditions of the Creative Commons Attribution (CC BY) license (<https://creativecommons.org/licenses/by/4.0/>).

1. Introduction

A vane pump is a type of displacement pump that works by regularly changing the volume of a sealed working chamber. Compared to other structured pump types, the vane pump has the benefits of a compact structure, uniform flow rate and low rotor inert. It is widely employed in petrochemical, aerospace, metallurgical and other fields [1,2]. Figure 1 depicts the structure of a double-acting vane pump. The pump rotor is concentrically attached to the stator; the vanes are radially installed in the rotor slots; and the rotor glides back and forth in the places as it rotates with the main shaft. The cavity is formed by the rotor, vane, stator inner cavity surface and pump end face. In the first half of the rotation of the rotor, a vacuum is formed in the pump and the liquid is sucked in; when the volume of the cavity is reduced from the maximum value to the minimum value, the liquid medium is pressed out. The media transfer is completed by periodic adjustments in the volume cavity [3].

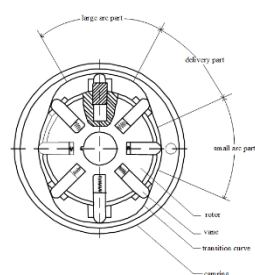


Figure 1. Vane pump cross-sectional configuration.

With the trend toward low noise and low pulsation in vane pumps, the classic vane pump's long-term vibration, noise, durability and other lingering difficulties must be

addressed [4], particularly noise and vibration. The pulsation of the pump output and pressure is propagated to all components of the hydraulic system, including the hydraulic hose and valves [5,6].

The noise is mainly created by the pressure pulsation, the stator curve structure and the working chamber pressure rise in three aspects [7], whereas the vibration is primarily caused by the flow pulsation caused by leakage and the impact vibration between the vane and the stator curve's two elements. As a result, a proper design of the stator curve structure and the construction of the vane pump's force model are critical to reducing noise and vibration and increasing the pump's dynamic performance. The dynamic performance of the pump has been explored in a few related articles.

One of the origins of vibration in vane pumps is the imbalance forces, which increase the amplitude as the manufacturing errors rise [8]. Numerical approaches have been demonstrated to predict pump vibrations, particularly those generated by hydrodynamic forces. This technique, which may be used in the initial design phase [9], can reduce the computational effort and enhance development efficiency. Pump vibration can also be caused by the guiding vane of an axial flow pump. It was discovered that an appropriate number of guide vanes has a role in suppressing the pressure fluctuations and vibroacoustics of axial pumps by comparing the radiated noise field stimulated by diffusers with the varied numbers of vanes [10]. Experiments have also revealed that different vane leading edge forms alter vane pump vibrations, and a method for determining the degree of cavitation behavior has been developed. As a result, a measurement system with a pump and sensors was designed to successfully eliminate the cavitation phenomena when the pump is operated [11]. To forecast the vibration characteristics of a multistage rotor system, a novel axial dynamic model integrating the transient force of the balance disk was presented, which can serve as a reference for the axial vibration model of a multistage pump rotor system [12]. Meanwhile, a two-way iterative fluid–structure coupling-based technique is presented to analyze the vibration characteristics of axial flow pumps. The fluid–structure coupling interaction has received less attention. The apparent time-frequency law of fluid pressure pulsation and structure vibration is given [13].

Meanwhile, other researchers optimized pump vibration and noise, leading to developing a multi-objective experimental and response surface-based optimization strategy for improving centrifugal pump hydroacoustic performance. The ideal combination of parameters for the synergistic optimization of hydraulic performance and noise was established using a multiple regression response surface model, which might result in a 3.03 percent gain in hydraulic efficiency and a 3.01 percent reduction in noise [14]. The results show that the radiation noise has typical dipole characteristics, and its directionality varies with the flow rate. A hybrid numerical method was proposed to obtain the streamwise noise source for the radiation noise of centrifugal pumps; the finite element method was used to obtain the acoustic simulation results, and the numerical method was verified by experiments [15]. Simulating the force situation of the components under various dynamic conditions using computational fluid dynamics (CFD) software COMSOL, some scholars proposed a new type of cylindrical vane pump by deriving the displacement calculation formula based on the design structure of the cylindrical vane pump, deriving the theoretical stator internal surface equation and establishing a three-dimensional model and using CFD software COMSOL to simulate the force situation of the components under various dynamic conditions [16]. The candidate transition curve functions for the stator with triangular and polynomial forms have also been discussed, and the V-A-J method (which converts the shape optimization task into a parameter value optimization task) has been used to find the best candidate for the “velocity criterion” and “acceleration criterion” curve equations. Without considering the effect of fluid movement, the dynamic features of the transition curves were investigated, and the findings revealed that different stator curves are acceptable for various applications [17].

Although these studies aid in understanding the source of vibration and noise in the vane pump, there is less research in the form of a high-dimensional curve stator curve of

the vane pump generated by vibration optimization. This work is based on a balanced eight-dimensional stator curve vane pump, the vane of the vane pump force analysis. Few people consider the effect of the ratio of large to small arc radius of the stator cavity on the performance of the transition curve. Especially in the process of constructing the derivation of higher order equations, the difference between the radius of large and small arcs directly affects the dynamic characteristics of the curve as the coefficient of the transition curve, which in turn affects the motion form of the vane, the contact state. Therefore, a reasonable stator curve is crucial to the performance of the vane pump. In this paper, we will combine the vane force analysis and consider the design requirements to optimize the large and small arc radius ratio of the stator inner cavity curve of double acting sliding vane pump by intelligent algorithm to get the optimal large and small arc radius ratio under the constraint condition.

The vibration noise during the operation of the vane pump and the stator inner cavity transition curve part of the wear are significant, as shown in Figure 2, and the size of the arc part has almost no scratch, according to the experiments. Each force on the slider is related to the octant of the stator curve, and the boundary condition of the octant is set with $R - r$ and the angle δ of the transition curve section; in this vane pump design, $R/r = 39/32 = 1.21875$, and the stator inner cavity transition curve part of the wear is serious. The stator inner cavity length and short radius ratio must be optimized, as indicated by the red outlined area in Figure 2.

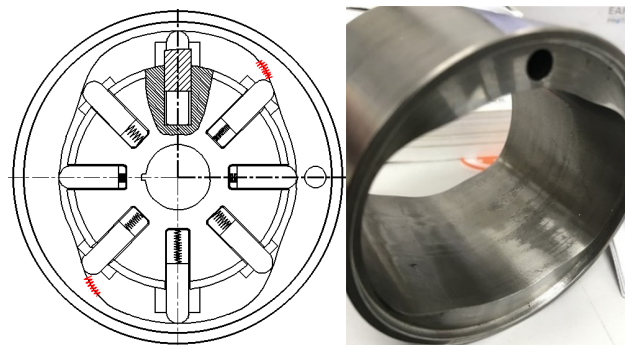


Figure 2. Stator wear location diagram.

2. Establishment of the Blade Force Model's Objective Function

Because there are apparent cut marks on the stator inner cavity surface transition curve of the pump after the experiment, consider the sliding friction between the vane and the wall as the objective function of optimization, and the value of R and r is the optimized result when the friction force is reduced to the minimum value.

The force analysis of the blade in the transition curve section is shown in Figure 3 [18].

In the transition curve section, the blades are exposed to centrifugal force F_i , spring force F_t , inertia force F_m , friction force F_f between the stator cavity and the stator, Coe-type inertia force F_k , viscous friction force F_η , contact reaction force F_{n1} , F_{n2} of the rotor and hydraulic pressure F_{p1} , F_{p2} , F_{p3} , F_{p4} , F_{p5} . Each force's angular function is illustrated below.

- (1) The centrifugal force of the blade as a function of the rotation angle [19] is shown in Equation (1).

$$F_i(\theta) = \begin{cases} mv\omega^2(R - \lambda C) & \theta \in [0, 20^\circ] \& [160^\circ, 200^\circ] \& [340^\circ, 360^\circ] \\ mv\omega^2(\rho(\theta) - \lambda C) & \theta \in [20^\circ, 70^\circ] \& [110^\circ, 160^\circ] \& [200^\circ, 250^\circ] \& [290^\circ, 340^\circ] \\ mv\omega^2(r - \lambda C) & \theta \in [70^\circ, 110^\circ] \& [250^\circ, 290^\circ] \end{cases} \quad (1)$$

where λc is the blade center of mass to the stator cavity distance, m_v is the rotating blade center mass, ω is the spindle angular velocity, R is the stator cavity large arc radius, r is the stator cavity small arc radius, $\rho(\theta)$ is the vector diameter of the blade.

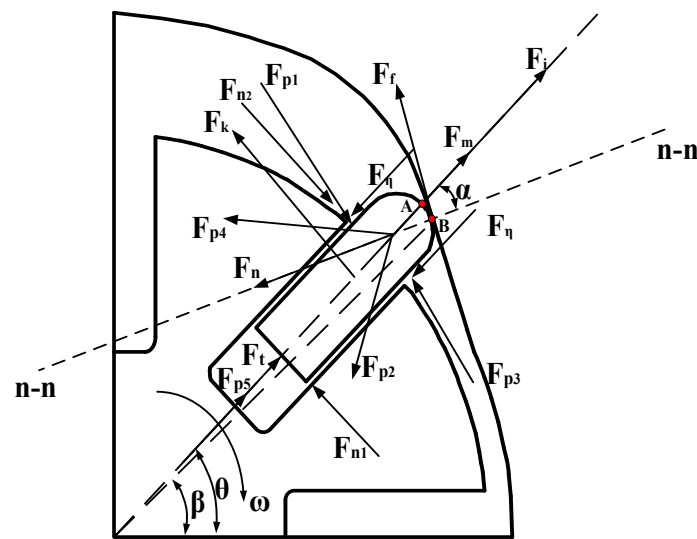


Figure 3. Blade transition cavity force analysis diagram.

(2) The spring force on the blade as a function of the angle of rotation is shown in Equation (2).

$$F_t(\theta) = \begin{cases} k(\mu - 15) & \theta \in [0, 20^\circ] \& [160^\circ, 200^\circ] \& [340^\circ, 360^\circ] \\ k(\mu - \rho(\theta) + 24) & \theta \in [20^\circ, 70^\circ] \& [110^\circ, 160^\circ] \& [200^\circ, 250^\circ] \& [290^\circ, 340^\circ] \\ k(\mu - 8) & \theta \in [70^\circ, 110^\circ] \& [250^\circ, 290^\circ] \end{cases} \quad (2)$$

where k is the spring stiffness factor, and μ is the spring free length.

(3) The inertia force on the blade as a function of the angle of rotation is shown in Equation (3).

$$F_m(\theta) = \begin{cases} m\omega^2 R = \frac{m\pi^2 n^2}{900} R & \theta \in [0, 20^\circ] \& [160^\circ, 200^\circ] \& [340^\circ, 360^\circ] \\ \frac{m\pi^2 n^2}{900} a(\theta) & \theta \in [20^\circ, 70^\circ] \& [110^\circ, 160^\circ] \& [200^\circ, 250^\circ] \& [290^\circ, 340^\circ] \\ m\omega^2 r = \frac{m\pi^2 n^2}{900} r & \theta \in [70^\circ, 110^\circ] \& [250^\circ, 290^\circ] \end{cases} \quad (3)$$

where m is the blade mass, n is the spindle speed, $a(\theta)$ is the radial acceleration of the blade in the transition curve section.

(4) The frictional force between the blade and the inner cavity of the stator as a function of the rotation angle is shown in Equation (4).

$$F_{trip}(\theta) = \begin{cases} m\omega^2 [R - \frac{L}{2}] \cdot \cos(90^\circ - \alpha) \cdot f & \theta \in [0, 20^\circ] \& [160^\circ, 200^\circ] \& [340^\circ, 360^\circ] \\ m\omega^2 [\rho(\theta) - \frac{L}{2}] \cdot \cos(90^\circ - \alpha) \cdot f & \theta \in [20^\circ, 70^\circ] \& [110^\circ, 160^\circ] \& [200^\circ, 250^\circ] \& [290^\circ, 340^\circ] \\ m\omega^2 [r - \frac{L}{2}] \cdot \cos(90^\circ - \alpha) \cdot f & \theta \in [70^\circ, 110^\circ] \& [250^\circ, 290^\circ] \end{cases} \quad (4)$$

where L is the blade length, α is the pressure angle formed by the blade and the stator cavity surface, and f is the friction coefficient.

(5) The Coe-type inertia force on the blade as a function of the rotation angle [20] is shown in Equation (5).

$$F_k(\theta) = \begin{cases} 2m\omega^2 [R - \frac{L}{2}] & \theta \in [0, 20^\circ] \& [160^\circ, 200^\circ] \& [340^\circ, 360^\circ] \\ 2m\omega V(\theta) \cdot \sin[\omega, V(\theta)] & \theta \in [20^\circ, 70^\circ] \& [110^\circ, 160^\circ] \& [200^\circ, 250^\circ] \& [290^\circ, 340^\circ] \\ 2m\omega^2 [r - \frac{L}{2}] & \theta \in [70^\circ, 110^\circ] \& [250^\circ, 290^\circ] \end{cases} \quad (5)$$

where $V(\theta)$ is the radial velocity of the blade in the transition curve section.

(6) The viscous friction force on the blade as a function of the rotation angle is shown in Equation (6).

$$F_{\eta}(\theta) = \begin{cases} \eta\omega(R - \frac{L}{2})[\frac{A_{vr1}}{h_{vr}} - \frac{A_{vs}}{h_{vs}}] & \theta \in [0, 20^{\circ}] \& [160^{\circ}, 200^{\circ}] \& [340^{\circ}, 360^{\circ}] \\ \eta V(\theta)[\frac{A_{vr}}{h_{vr}} - \frac{A_{vs}}{h_{vs}}] & \theta \in [20^{\circ}, 70^{\circ}] \& [110^{\circ}, 160^{\circ}] \& [200^{\circ}, 250^{\circ}] \& [290^{\circ}, 340^{\circ}] \\ \eta\omega(r - \frac{L}{2})[\frac{A_{vr2}}{h_{vr}} - \frac{A_{vs}}{h_{vs}}] & \theta \in [70^{\circ}, 110^{\circ}] \& [250^{\circ}, 290^{\circ}] \end{cases} \quad (6)$$

where η is the oil viscosity, A_b is the actual contact area between the bottom of the blade and the oil according to the design size of the blade, A_{vs} is the actual contact area between the blade and the end plate, A_{vr1} is the actual contact area between the large circular arc section blade and the rotor, A_{vr2} is the actual contact area between the small circular arc section blade and the rotor, the actual contact area between the blade and the rotor in the stator transition curve section $A_{vr} = 65 * [46 - \rho(\theta)]$. h_{vr} is the clearance between the blade and the rotor, h_{vs} is the clearance between the blade and the end plate.

(7) The contact reaction force on the blade by the rotor is shown in Equation (7) as a function of the rotation angle.

$$F_N(\theta) = \begin{cases} F_{N1} = \frac{\xi \cdot L_1 (f \cos \alpha - \sin \alpha) + (L_1 - L/2) F_k(\theta)}{L - L_1} \\ F_{N2} = \frac{\xi \cdot L (f \cos \alpha - \sin \alpha) + L/2 \cdot F_k(\theta)}{L - L_1} \end{cases} \quad \theta \in [0, 360^{\circ}] \quad (7)$$

where L_1 is the length of the blade extending outside the rotor slot, L is the length of the blade, and ξ is the coefficient of the contact reaction force on the blade by the rotor.

(8) The hydraulic pressure on the blade as a function of the turning angle is shown in Equation (8).

$$F_p(\theta) = \begin{cases} F_{p1} = a_1 \cdot \sin(b_1 \theta + C_1) + \\ \quad a_2 \cdot \sin(b_2 \theta + C_2) + a_3 \cdot \sin(b_3 \theta - C_3) \\ F_{p2} = a_4 \cdot \sin(b_4 \theta - C_4) + \\ \quad a_5 \cdot \sin(b_5 \theta + C_5) + a_6 \cdot \sin(b_6 \theta + C_6) \\ F_{p3} = a_7 \cdot \sin(b_7 \theta - C_7) + \\ \quad a_8 \cdot \sin(b_8 \theta - C_8) + a_9 \cdot \sin(b_9 \theta + C_9) \\ F_{p4} = a_{10} \cdot \sin(b_{10} \theta + C_{10}) + \\ \quad a_{11} \cdot \sin(b_{11} \theta + C_{11}) + a_{12} \cdot \sin(b_{12} \theta + C_{12}) \\ F_{p5} = 41840158.12N \end{cases} \quad \theta \in [20^{\circ}, 70^{\circ}] \& [110^{\circ}, 160^{\circ}] \& [200^{\circ}, 250^{\circ}] \& [290^{\circ}, 340^{\circ}] \quad (8)$$

where the blade is subjected to the various hydraulic component forces by design of experiment (DOE) simulation results for fitting the way to establish the individual component forces as follows. The function equation of the hydraulic pressure on the slide is detailed in Appendix A.

The blade rotation angle as a function of the hydraulic pressure at the wall of the pressure chamber is shown in Equation (9).

$$F_{p1}(\theta) = a_1 \cdot \sin(b_1 \cdot \theta + c_1) + a_2 \cdot \sin(b_2 \cdot \theta + c_2) + a_3 \cdot \sin(b_3 \cdot \theta + c_3) \quad (9)$$

$$\begin{aligned} a_1 &= 9.277 \times 10^5 & (-4.131 \times 10^8, 4.15 \times 10^8) \\ b_1 &= 0.0597 & (-8.295, 8.415) \\ c_1 &= 0.255 & (-403.3, 403.8) \\ a_2 &= 5.412 \times 10^5 & (-4.329 \times 10^8, 4.34 \times 10^8) \\ b_2 &= 0.088 & (-11.26, 11.43) \\ c_2 &= 2.063 & (-482.6, 486.7) \\ a_3 &= 4.692 \times 10^4 & (-1.088 \times 10^6, 1.182 \times 10^6) \\ b_3 &= 0.2742 & (-1.396, 1.944) \\ c_3 &= -1.033 & (-52.72, 50.65) \end{aligned}$$

The blade rotation angle as a function of the hydraulic pressure on the circular surface of the oil pressure chamber is shown in Equation (10).

$$F_{p2}(\theta) = a_4 \cdot \sin(b_4 \cdot \theta + c_4) + a_5 \cdot \sin(b_5 \cdot \theta + c_5) + a_6 \cdot \sin(b_6 \cdot \theta + c_6) \quad (10)$$

$$\begin{aligned} a_4 &= 4.109 \times 10^6 & (-1.808 \times 10^{11}, 1.808 \times 10^8) \\ b_4 &= 0.1298 & (-443.2, 443.4) \\ c_4 &= -1.872 & (-1.493 \times 10^4, 1.492 \times 10^4) \\ a_5 &= 9.939 \times 10^6 & (-4.512 \times 10^{11}, 4.512 \times 10^{11}) \\ b_5 &= 0.1598 & (-1068, 1068) \\ c_5 &= 0.2701 & (-3.534 \times 10^4, 3.534 \times 10^4) \\ a_6 &= 6.122 \times 10^6 & (-6.32 \times 10^{11}, 6.32 \times 10^{11}) \\ b_6 &= 0.177 & (-625.6, 626) \\ c_6 &= 2.845 & (-2.063 \times 10^4, 2.063 \times 10^4) \end{aligned}$$

The blade rotation angle as a function of the liquid pressure at the wall of the suction chamber is shown in Equation (11).

$$F_{p3}(\theta) = a_7 \cdot \sin(b_7 \cdot \theta + c_7) + a_8 \cdot \sin(b_8 \cdot \theta + c_8) + a_9 \cdot \sin(b_9 \cdot \theta + c_9) \quad (11)$$

$$\begin{aligned} a_7 &= 1.615 \times 10^6 & (-1.544 \times 10^{10}, 1.545 \times 10^{10}) \\ b_7 &= 0.1021 & (-85.82, 86.03) \\ c_7 &= -1.336 & (-3091, 3089) \\ a_8 &= 3.58 \times 10^6 & (-1.156 \times 10^{11}, 1.156 \times 10^{11}) \\ b_8 &= 0.131 & (-370.9, 371.2) \\ c_8 &= 0.8403 & (-1.161 \times 10^4, 1.161 \times 10^4) \\ a_9 &= 2.279 \times 10^6 & (-1.311 \times 10^{11}, 1.311 \times 10^{11}) \\ b_9 &= 0.1435 & (-274.4, 274.7) \\ c_9 &= 3.598 & (-8224, 8231) \end{aligned}$$

The blade rotation angle as a function of the fluid pressure at the circular arc of the suction chamber is shown in Equation (12).

$$F_{p4}(\theta) = a_{10} \cdot \sin(b_{10} \cdot \theta + c_{10}) + a_{11} \cdot \sin(b_{11} \cdot \theta + c_{11}) + a_{12} \cdot \sin(b_{12} \cdot \theta + c_{12}) \quad (12)$$

$$\begin{aligned} a_{10} &= 7.522 \times 10^5 & (2.657 \times 10^5, 1.239 \times 10^6) \\ b_{10} &= 0.03875 & (-0.002936, 0.08044) \\ c_{10} &= 0.3424 & (-1.531, 2.215) \\ a_{11} &= 1.541 \times 10^5 & (-1.575 \times 10^6, 1.883 \times 10^6) \\ b_{11} &= 0.219 & (-0.8047, 1.243) \\ c_{11} &= 0.309 & (-29.13, 29.75) \\ a_{12} &= 2.349 \times 10^5 & (-1.531 \times 10^6, 2.001 \times 10^6) \\ b_{12} &= 0.3297 & (-0.2796, 0.9391) \\ c_{12} &= 0.2197 & (-18.26, 18.7) \end{aligned}$$

The contact angle and rotation angle function equations are as follows. MATLAB was used to fit the function equation of the blade contact angle α and the rotation angle θ by sampling ten coordinate points [21]. After comparing various types of suitable approximation methods, it was discovered that the Gaussian approximation method was the closest to the resultant data, so the function equation of the blade contact angle and the rotation angle was fitted by this method as follows. The functional relationship between the contact angle of the arc top profile of the sliding plate and the rotation angle of the sliding plate is described in detail in Appendix B.

The Gaussian approximation method generic function model is shown in Equation (13).

$$f(x) = a_1 \cdot \exp\left(-((x - b_1)/c_1)^2\right) \quad (13)$$

The coefficient (95% confidence level) is as follows.

$$\begin{aligned} a_1 &= 48.11 & (46.15, 50.07) \\ b_1 &= 27.1 & (26.64, 27.57) \\ c_1 &= 13.89 & (13.27, 14.55) \end{aligned}$$

The results are showed in Equation (14).

$$\alpha = 48.11 \cdot \exp\left(-((\theta - 27.1)/13.89)^2\right) \quad (14)$$

To make it easier to develop the equation of the force on the slider as a function of the slider rotation angle, the relationship between the slider rotation angle θ and the contact angle α of the stator is determined.

As the blade and stator cavity mutual wear situation is serious, fully consider the blade force situation, the blade and stator inner wall between the minimum value of the sliding friction as the optimization objective function. Additionally, the calculation formula of sliding friction is $F_f = f \cdot F_n$, according to Figure 4 force analysis, to obtain the force balance sketch in the direction of the common normal, combined with the actual force situation of the vane pump to obtain the blade by each force, according to the sliding friction formula to find the reverse support force F_n on the wall surface of the blade.

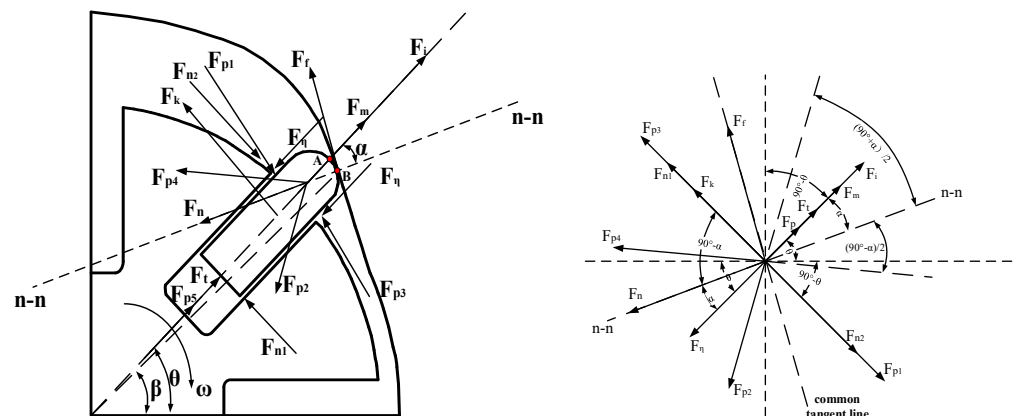


Figure 4. Slider transition chamber force analysis diagram.

The equation of force balance in the direction of the common normal is shown in Equation (15).

$$F_n + F_\eta \cdot \cos\alpha + (F_{n1} + F_k + F_{p3}) \cdot \cos(90^\circ - \alpha) - (F_{n2} + F_{p1}) \cdot \cos(90^\circ - \alpha) - (F_{p5} + F_k + F_i) \cdot \cos\alpha + F_{p4} \cdot \cos\left(\frac{90^\circ - \alpha}{2}\right) + F_{p2} \cdot \cos\left(\frac{90^\circ + \alpha}{2}\right) = 0 \quad (15)$$

The collation yields Equation (16).

$$F_n = (F_{p5} + F_k + F_i - F_\eta) \cdot \cos\alpha + (F_{n2} + F_{p1} - F_{p3} - F_{n1} - F_k) \cdot \cos(90^\circ - \alpha) - F_{p4} \cdot \cos\left(\frac{90^\circ - \alpha}{2}\right) - F_{p2} \cdot \cos\left(\frac{90^\circ + \alpha}{2}\right) \quad (16)$$

The resulting sliding friction relationship between the slider and the stator cavity is shown in Equations (17) and (18).

$$F_f = f \cdot F_n = f \cdot \left[\begin{aligned} &(F_{p5} + F_k + F_i - F_\eta) \cdot \cos\alpha + (F_{n2} + F_{p1} - F_{p3} - F_{n1} - F_k) \cdot \cos(90^\circ - \alpha) \\ &- F_{p4} \cdot \cos\left(\frac{90^\circ - \alpha}{2}\right) - F_{p2} \cdot \cos\left(\frac{90^\circ + \alpha}{2}\right) \end{aligned} \right] \quad (17)$$

$$F_f = f \cdot F_n = f \cdot \left[\begin{array}{l} \left(F_{p5} + k \cdot (\mu - \rho(\theta) + 24) + m \cdot \omega^2 (\rho(\theta) - \lambda c) - \eta V(\theta) \left[\frac{A_{vr}}{h_{vr}} - \frac{A_{vs}}{h_{vs}} \right] \right) \cdot \cos \alpha + \cos(90^\circ - \alpha) \cdot \\ \left(\frac{\xi \cdot [L \cdot (f \cdot \cos \alpha - \sin \alpha) + (L/2) \cdot F_k(\theta) - (L_1 \cdot (f \cdot \cos \alpha - \sin \alpha) + (L_1 - L/2) \cdot F_k(\theta))]}{L - L_2} + F_{p1} - F_{p3} - \right) \\ 2m\omega \cdot V(\theta) \\ -F_{p4} \cdot \cos\left(\frac{90^\circ - \alpha}{2}\right) - F_{p2} \cdot \cos\left(\frac{90^\circ + \alpha}{2}\right) \end{array} \right] \quad (18)$$

which $A_{vr} = 65 * [46 - \rho(\theta)]$ and $\xi = \frac{(F_p + F_i - F_m)(L - L_1) - L_1 f F_k(\theta)}{[(f^2 + 1)L + (f^2 - 1)L_1] \cos \alpha - 2L_1 f \sin \alpha}$.

The remaining values of each parameter are shown in Table 1.

Table 1. Table of parameter values.

A_b (mm ²)	A_{vs} (mm ²)	A_{vr1} (mm ²)	A_{vr2} (mm ²)	η (mm ² /s)	h_{vr} (mm)	h_{vs} (mm)
340.58	80.03	423.54	910	30	0.03	0.30

The comprehensive values above can be obtained and will be the slide and the stator cavity of the minimum value of the sliding friction of the objective function relationship, as shown in Equation (19).

$$\min F_f = f \cdot F_n = f \cdot \left[\begin{array}{l} \left(F_{p5} + k \cdot (\mu - \rho(\theta) + 24) + m \cdot \omega^2 (\rho(\theta) - \lambda c) - \eta V(\theta) \left[\frac{A_{vr}}{h_{vr}} - \frac{A_{vs}}{h_{vs}} \right] \right) \cdot \cos \alpha + \cos(90^\circ - \alpha) \cdot \\ \left(\frac{\xi \cdot [L \cdot (f \cdot \cos \alpha - \sin \alpha) + (L/2) \cdot F_k(\theta) - (L_1 \cdot (f \cdot \cos \alpha - \sin \alpha) + (L_1 - L/2) \cdot F_k(\theta))]}{L - L_2} + F_{p1} - F_{p3} - \right) \\ 2m\omega \cdot V(\theta) \\ -F_{p4} \cdot \cos\left(\frac{90^\circ - \alpha}{2}\right) - F_{p2} \cdot \cos\left(\frac{90^\circ + \alpha}{2}\right) \end{array} \right] \quad (19)$$

3. Stator Inner Cavity Curve Length and Radius Optimization

Eberhart and Kennedy proposed that the particle swarm optimization (PSO) algorithm consists of a series of iterative forms shown in Equations (20) and (21), iterating the velocity magnitude and direction of travel at times until the termination condition is reached [22].

$$V_{i,j}(t+1) = \omega V_{i,j}(t) + C_1 R \text{ and } [P_{i,j} - x_{i,j}(t)] + C_2 R \text{ and } [P_{i,j} - x_{i,j}(t)] \quad (20)$$

$$x_{i,j}(t+1) = x_{i,j}(t) + V_{i,j}(t+1) \quad (i, j = 1, 2, \dots, d) \quad (21)$$

where ω is the inertia weight factor, C_1 and C_2 are learning elements with values in the range between 0 and 2, and rand and Rand are two mutually independent random functions following $U(0,1)$. C_1 is the particle's distance from its optimal position step, C_2 is the particle's distance from the global optimal position step, and $C_1 = C_2 = 1.49445$ is taken in the requested objective function.

Constraints on the optimization of the stator length and radius parameters. The objective function of minimizing the sliding friction between the slider and the stator cavity is solved by the intelligent particle swarm algorithm, and some constraints still need to be set to make the solution converge more easily and find the optimal solution according to the design requirements and size limitations [23]. The constraints are shown in Table 2.

Table 2. Constraints.

α	ω (rad/s)	f	α	r (mm)	R (mm)	R/r ($R \neq r$)
50°	100	0.13	[0, 90°]	[32, 34]	[32, 40]	(1, 1.2603]

We solve the objective function with constraints according to the particle swarm algorithm.

- (1) When $R - r = 1$, the minimum value of the objective function is 4.8298×10^6 , at which time $R = 33, r = 32, \theta = 26.65^\circ$.
- (2) When $R - r = 2$, the minimum value of the objective function is 4.4148×10^6 , when $R = 34, r = 32, \theta = 24.56^\circ$.
- (3) When $R - r = 3$, the minimum value of the objective function is 4.0240×10^6 , when $R = 35, r = 32, \theta = 23.71^\circ$.
- (4) When $R - r = 4$, the minimum value of the objective function is 3.6583×10^6 , when $R = 36, r = 32, \theta = 22.90^\circ$.
- (5) When $R - r = 5$, the minimum value of the objective function is 3.3217×10^6 , when $R = 37, r = 32, \theta = 23.13^\circ$.
- (6) When $R - r = 6$, the minimum value of the objective function is 3.4313×10^6 , when $R = 38, r = 32, \theta = 22.14^\circ$.

The objective function value of the sliding friction between the slide and the stator cavity is minimized for $R = 37, r = 32$ and $\theta = 23.13^\circ$, as calculated by the particle swarm algorithm analysis. The simulation results are shown in Figures 5 and 6.

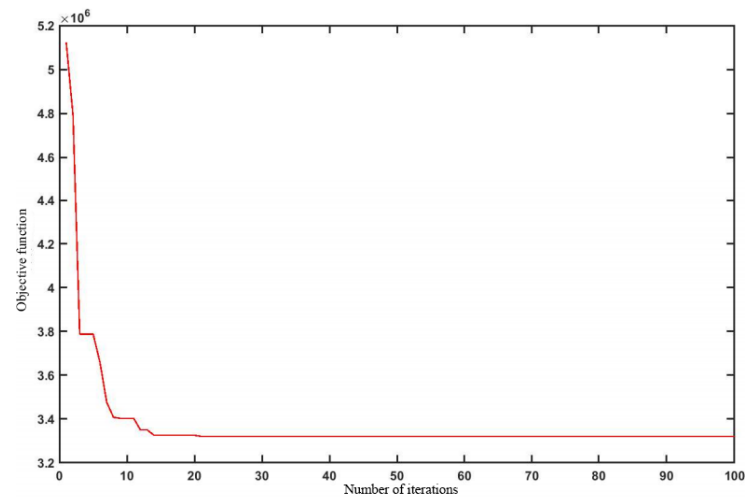


Figure 5. Optimized minimum value of sliding friction.

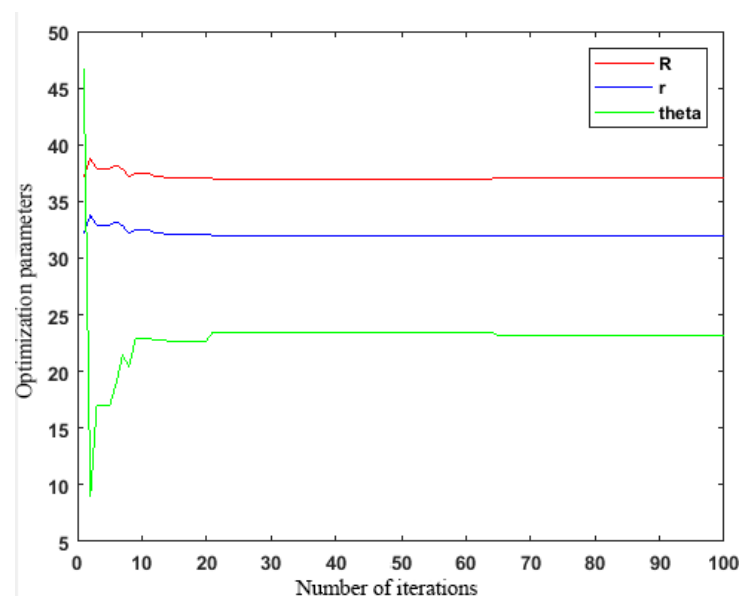


Figure 6. Optimized values of R, r and θ .

The optimized results $R = 37$, $r = 32$ are brought into the octant curve simulation program. The comparison results before and after the optimization of the stator cavity transition curve can be obtained by the simulation program, as shown in Figure 7.

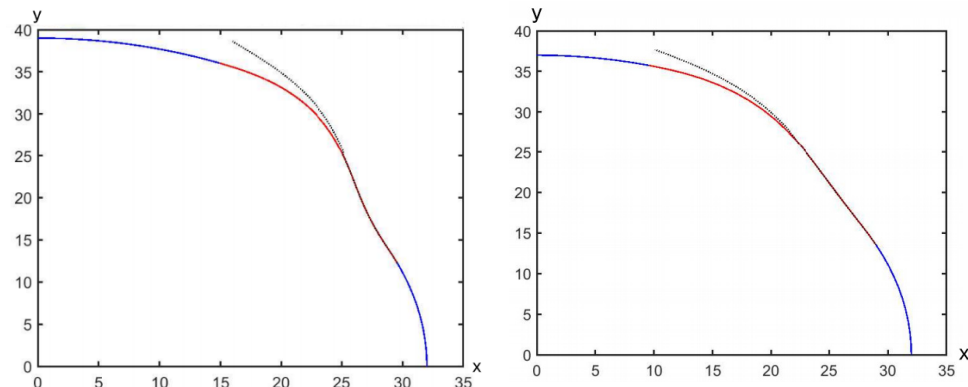


Figure 7. Stator cavity transition curve optimization comparison chart.

4. Results

Based on the stator model before and after optimization, the ADAMS dynamics simulation of the virtual prototype before and after stator optimization is carried out to predict the effect of the optimized stator on pump kinematics and dynamics performance.

We created the simulation model in ADAMS/View, set up the working environment and set up the gravity, coordinate system, etc., as shown in Figure 8.

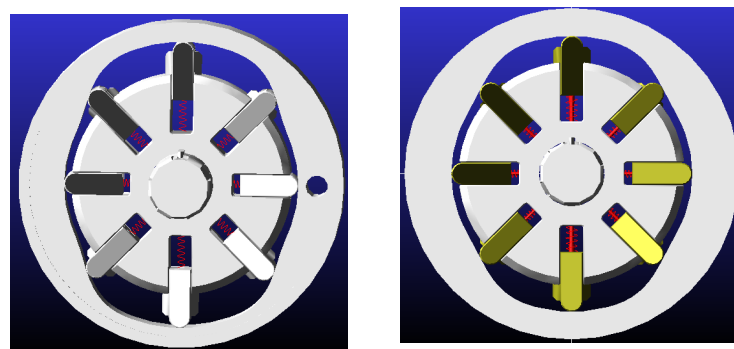


Figure 8. ADAMS model of sliding vane pump.

Spring force is applied between the blade and the rotor blade slot, friction force between the edge and the inner wall of the rotor blade slot. Solid-to-solid contact force is applied between the blade and the stator cavity and a force acting on the bottom and both sides of the edge, applying a given speed to the spindle, setting the simulated spindle speed to 300 rpm.

Sliding vane pump simulation results are compared and analyzed as follows.

- (1) Spindle torque curve before and after stator cavity length to radius ratio optimization.

Comparing Figures 9 and 10, it can be seen from the simulation curve that there is a prominent peak in the shaft torque before the optimization of the central stator cavity. This analysis is put forward because when the difference of $R - r$ is significant, a curve section with large curvature will be generated at the transition curve. Therefore, an ample torque is developed in this curve section when the main shaft rotates. The optimized simulation results show that the maximum value of the spindle torque is controlled within 5800 N·mm. Compared with the maximum torque peak of 16,000 N·mm before optimization, there is no prominent peak of the spindle torque in the whole rotation cycle. The optimization of the length and radius of the stator cavity has a good effect on reducing the spindle torque.

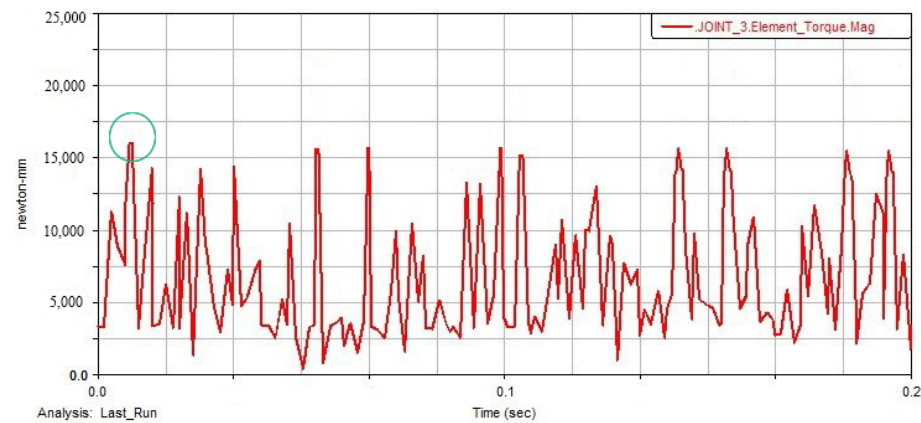


Figure 9. Comparison of spindle torque before stator optimization.

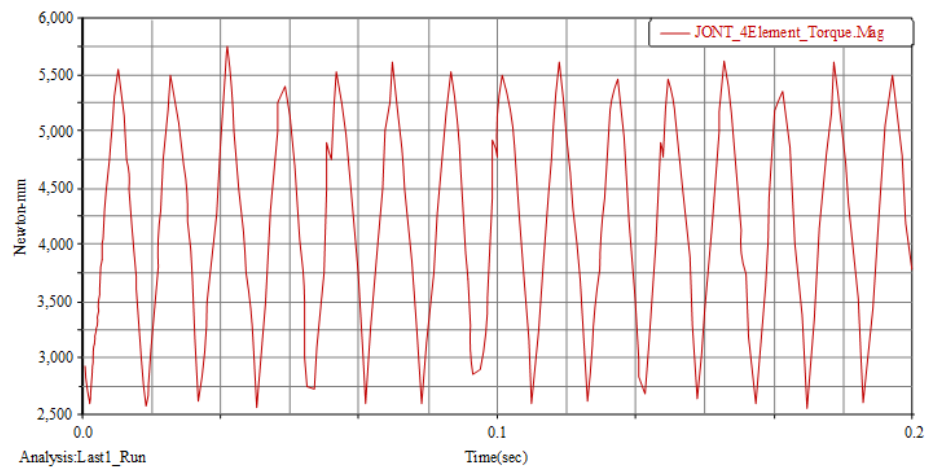


Figure 10. Comparison of spindle torque after stator optimization.

- (2) Slider acceleration curves before and after optimizing stator cavity length to radius ratio.

As shown in Figures 11 and 12, the simulation results before the optimization of the stator cavity show that the acceleration of the slide has a sudden change of the great peak; the reason is that when the difference of $R - r$ is significant, it will produce a curve section with large curvature at the transition curve. Therefore, when the slide slides on the stator transition curved surface, it will significantly impact this curve surface, resulting in severe wear and vibration. The simulation results of stator cavity optimization show that the maximum value of slide acceleration is controlled within $3.0 \times 10^5 \text{ mm/s}^2$ compared with the peak value of $5.0 \times 10^6 \text{ mm/s}^2$ before optimization; there is no significant peak value of slide acceleration in the whole rotation cycle, which shows that the optimization of the length and radius of stator cavity has a more significant effect on reducing the slide acceleration impact.

- (3) Friction curves between the slider and rotor slider slot before and after optimizing the stator cavity length and short radius ratio.

As shown in Figures 13 and 14, the simulation results before optimizing the stator cavity show that the friction between the slide and the rotor slider slot changed abruptly to a great peak. The reason is that when the difference of $R - r$ is significant, a curve section with large curvature will be generated at the transition curve. Therefore, when the slider slides on the stator transition curved surface, it will generate a large reaction force on the slider arc side, which will increase the pressure between the slider and the rotor slider slot wall, and the sliding friction will increase when the slider slides radially, resulting in deeper scratches. From the stator cavity optimization simulation results, it can be seen that

the friction force between the slider and the rotor slider slot is controlled within 0.0032 N. Compared with the peak friction force of 50 N between the slider and the rotor slider slot before optimization, there is no large peak friction force between the slider and the rotor slider slot during the whole rotation cycle.

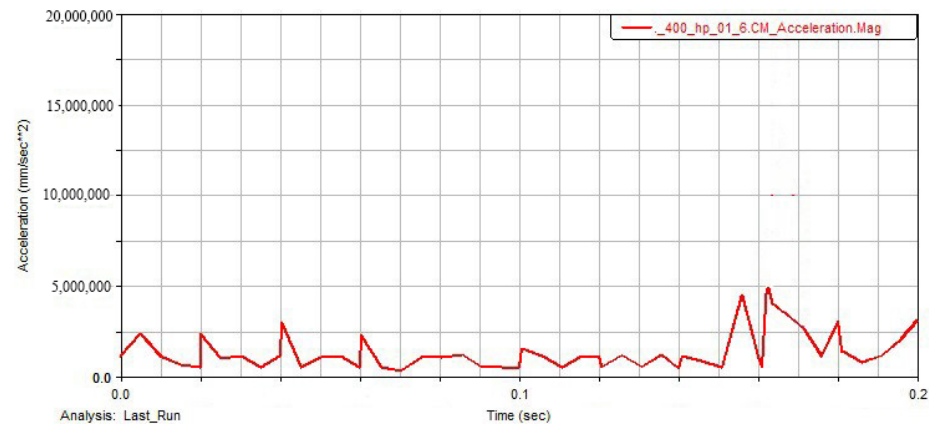


Figure 11. Comparison of slider acceleration before stator optimization.

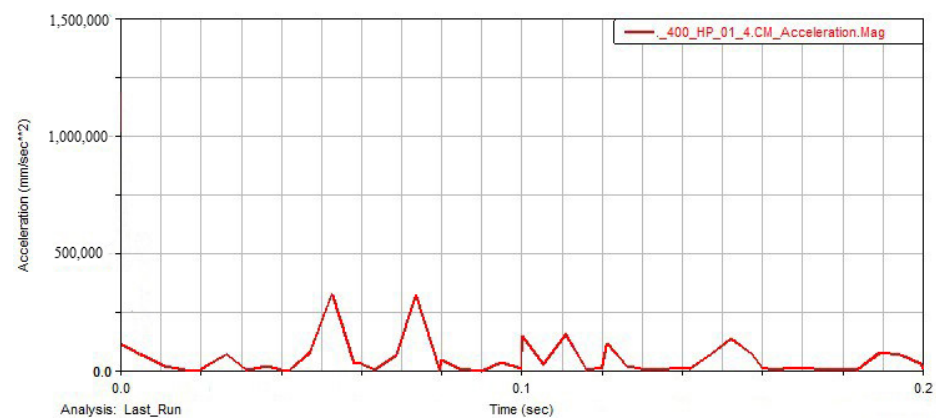


Figure 12. Comparison of slider acceleration after stator optimization.

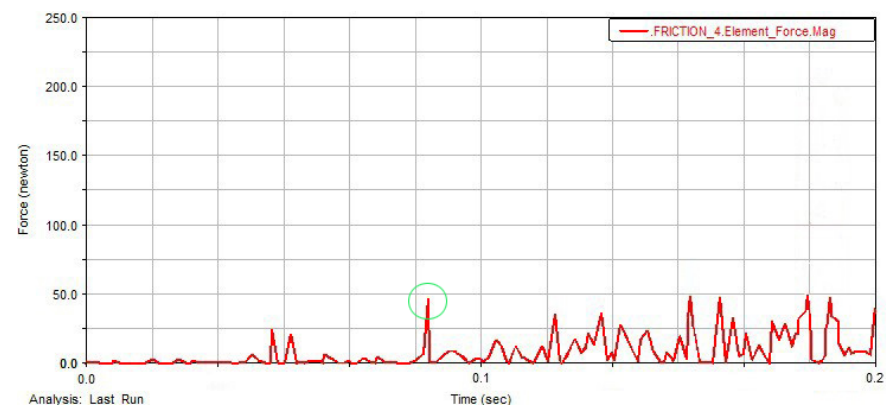


Figure 13. Comparison of friction between slider and rotor slider slot before stator optimization.

- (4) Slider–stator contact force curve before and after optimizing the stator cavity length to short radius ratio.

As shown in Figures 15 and 16, the simulation results before stator cavity optimization show that the contact force between the slide and the stator has a sudden and extreme peak because when the difference of $R - r$ is significant, a curve section with large curvature will be generated at the transition curve. As a result, when the slide slides on the stator

transition curved surface, it will produce an excellent acceleration impact on this curved surface. Then, the slide and the stator will have a great elastic deformation, resulting in a sudden change in the contact force and causing a severe wear phenomenon. The simulation results of the stator cavity optimization show that the maximum value of the contact force between the slider and the stator is controlled within 21 N. Compared with the peak value of the contact force between the slider and the stator before optimization, which reaches 75 N, the peak value of the contact force between the slider and the stator is significantly reduced during the whole rotation cycle, which indicates that the optimization of the length and radius of the stator cavity has a beneficial effect on reducing the contact force between the slider and the stator.

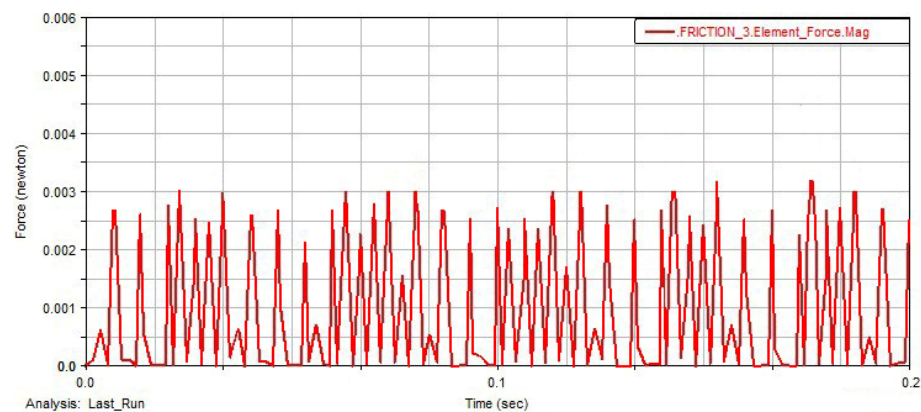


Figure 14. Comparison of friction between slider and rotor slider slot after stator optimization.

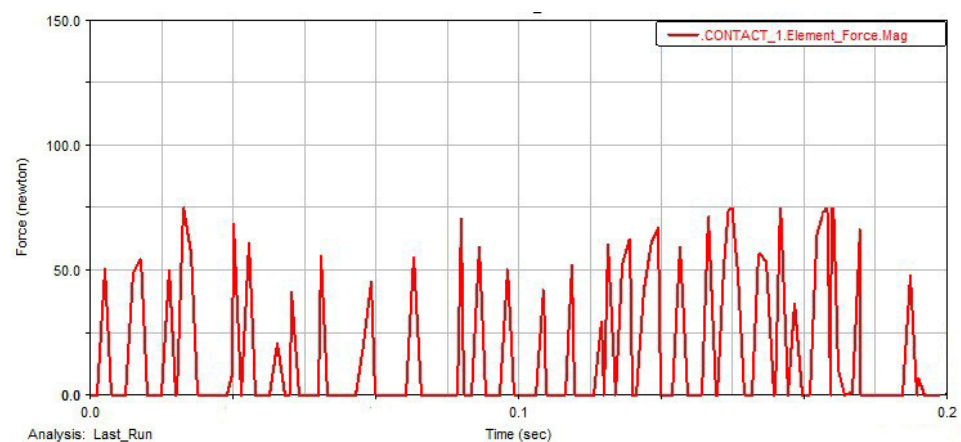


Figure 15. Comparison of slide and stator contact force before stator optimization.

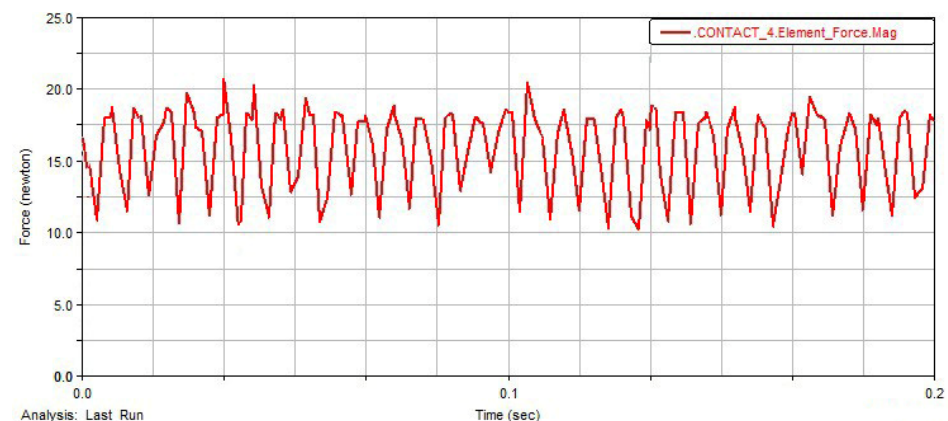


Figure 16. Comparison of slide and stator contact force after stator optimization.

From the ADAMS simulation results, it can be seen that the spindle torque, slider acceleration, blade and rotor friction, and blade and stator contact force numerical magnitude are reduced before and after stator optimization, indicating that the optimization of the length and radius of the stator inner cavity has a beneficial effect on lowering the blade and stator contact force.

5. Conclusions

With algorithm optimization and dynamics simulation of the transition curve of the stator cavity of the vane pump, the following research results were obtained.

1. The explicit expression of the blade contact angle as a function of the blade rotation angle was obtained by fitting the values of the sampling points. The analysis showed that the blade contact angle was maximum in the middle of the transition curve and that the Gaussian approximation method had a good approximation effect.
2. The optimization model of the long–short radius ratio using an intelligent particle swarm algorithm. According to the force balance equation, the expression of the sliding friction between the blade and the stator was derived. To minimize the sliding friction force on the edge, the optimized solution of the long–short radius ratio of the inner cavity of the stator was calculated.
3. The dynamics of the vane pump was simulated using Adams separately, and the main shaft torque, vane acceleration, vane and rotor friction, and vane and stator contact force before and after optimization were compared and analyzed. The results showed that the optimized stator performance was better.

Author Contributions: Conceptualization, D.X.; methodology, D.X.; software, S.L.; validation, D.X., J.W. and X.B.; formal analysis, D.X.; investigation, S.L.; data curation, D.X.; writing—original draft preparation, D.X.; writing—review and editing, D.X. and Y.S.; visualization, J.W. and X.B.; supervision, Y.S.; project administration, Y.S.; funding acquisition, Y.S. All authors have read and agreed to the published version of the manuscript.

Funding: The research is supported by Heilongjiang Province to support the transformation of major scientific and technological achievements project (Grant No. CG20A006); National Defense Basic Research Program Projects (Grant No. JCKY2019412D004).

Institutional Review Board Statement: Not applicable.

Informed Consent Statement: Not applicable.

Conflicts of Interest: The authors declare no potential conflict of interest with respect to the research, authorship and publication of this article.

Abbreviations

F_i	Centrifugal force
F_t	Spring force
F_m	Inertia force
F_k	Coe-type inertia force
F_η	Viscous friction force
F_{n1}, F_{n2}	Contact reaction force of the rotor
m_v	the rotating blade center mass
ω	the spindle angular velocity
R	the stator internal cavity large arc radius
r	the stator internal cavity small arc radius
$\rho(\theta)$	the blade vector diameter
k	the spring stiffness coefficient
μ	the spring free length
m	the blade mass

n	the spindle speed
F_f	Friction force between the stator cavity and the stator
λc	the distance between the vane center of mass and the stator inner cavity
$a(\theta)$	the radial acceleration of the blade in the transition curve section
L	the blade length
α	the pressure angle formed by the blade and the stator cavity surface
f	the friction coefficient
$V(\theta)$	the radial velocity of the blade in the transition curve section
η	the oil viscosity
A_b	the actual contact area between the bottom of the blade and the oil fluid according to the design size of the blade
A_{vs}	the actual contact area between the blade and the endplate
A_{vr1}	the actual contact area between the blade and the rotor in the sizeable circular arc section
A_{vr2}	the actual contact area between the blade and the rotor in the small circular arc section
A_{vr}	the actual contact area between the blade and the rotor in the stator transition curve section
h_{vr}	the clearance between the blade and the rotor
h_{vs}	the clearance between the blade and the endplate
L_1	the length of the blade extending outside the rotor slot
ξ	the coefficient of the contact reaction force of the edge by the rotor on the edge
$F_{p1}, F_{p2}, F_{p3}, F_{p4}, F_{p5}$	Hydraulic pressure

Appendix A

Since the hydraulic pressure on the suction cavity, pressure cavity wall surface and circular arc surface of the slide is changing with the rotation angle of the slide at all times during the rotation of the slide, the hydraulic pressure on the slide must be clarified as a function of the rotation angle during the force analysis of the slide and the stator cavity surface. Here, the finite element simulation method is used to derive the slider as a function of the change in the rotation angle.

The finite element solution sets the time step according to the different speed, and every 6° is 1 step—total 10 steps. The transition curve cavity slide fluid pressure results are analyzed as follows.

The force cloud diagram of the slide's hydraulic pressure in the transition curve cavity section is shown in Figure A1.

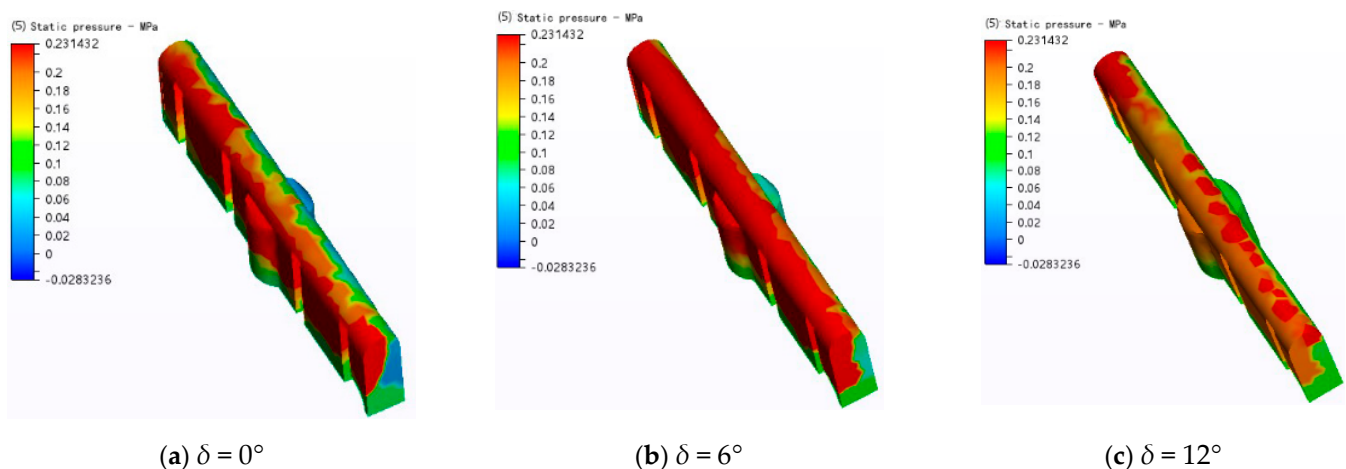


Figure A1. Cont.

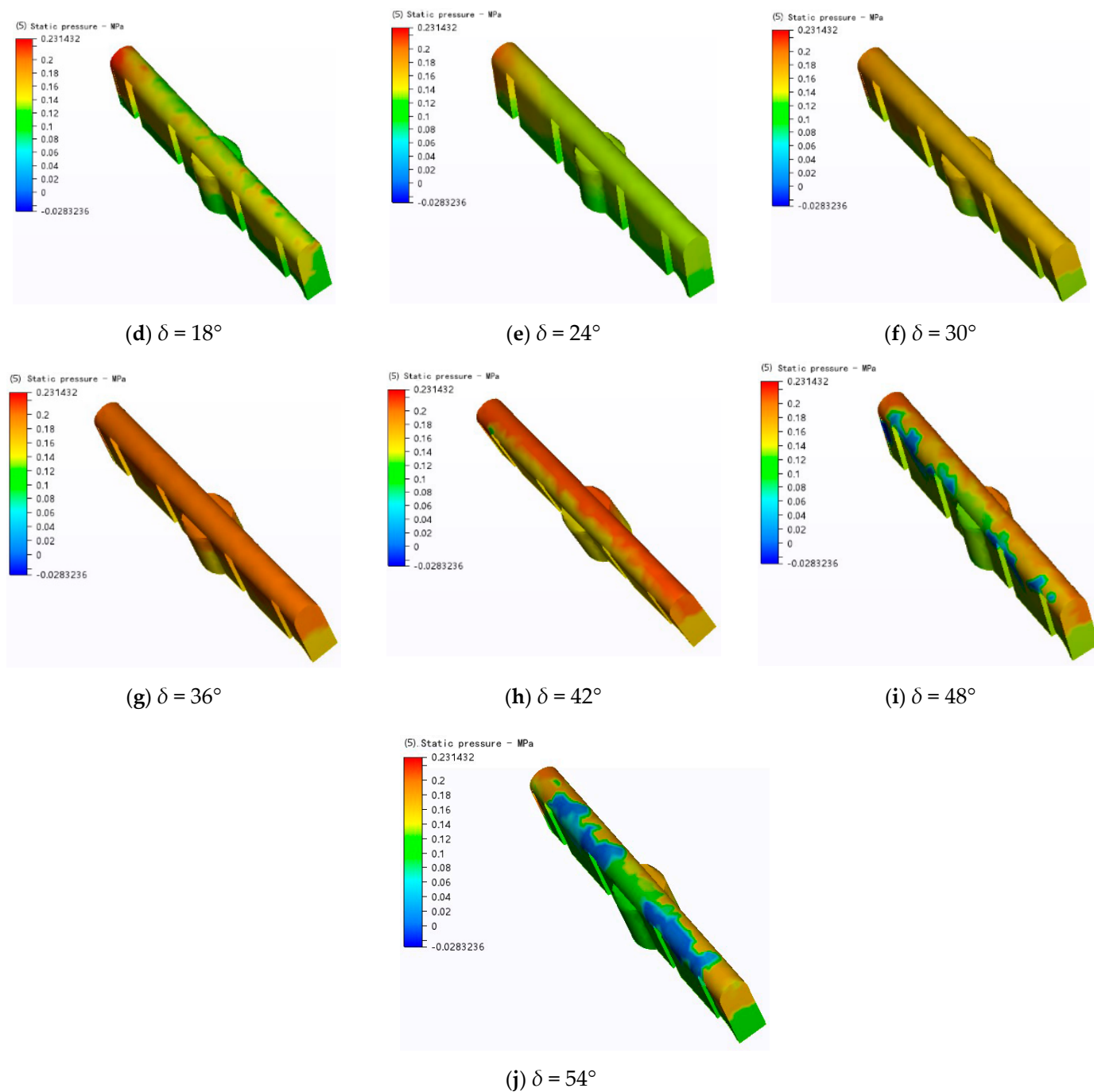


Figure A1. Fluid pressure nebulae of the model with different slide angles.

The force cloud diagram of the hydraulic pressure section of the slide in the transition curve cavity section is shown in Figure A2.

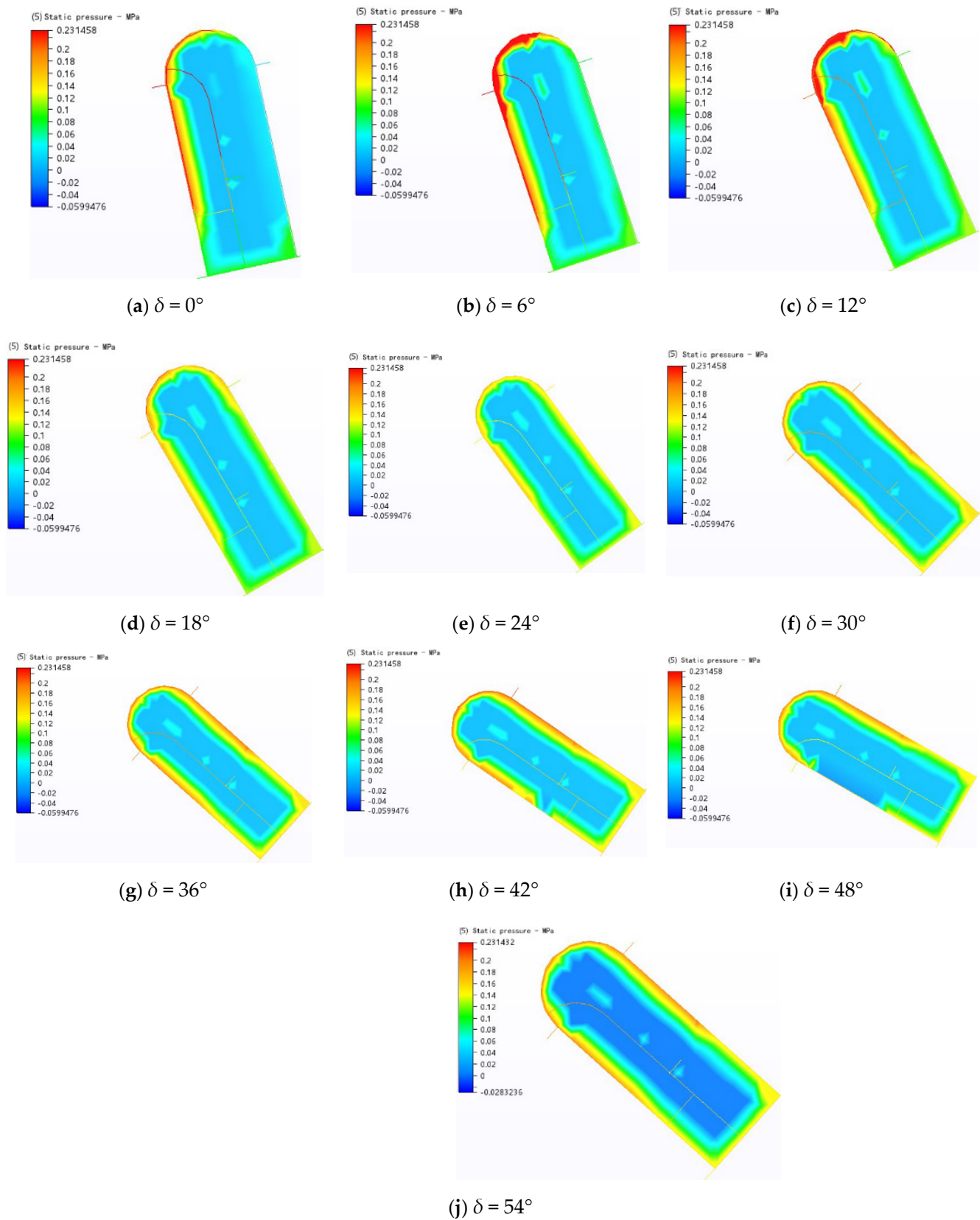


Figure A2. Fluid pressure nephogram under different slide angles.

(1) Material mechanics analysis of slide section

According to the principle of material mechanics, the slider hydraulic pressure cloud can be simplified to a cantilever beam structure for linear load distribution and uniform load analysis of the circular part of the slider. As shown in Figure A3.

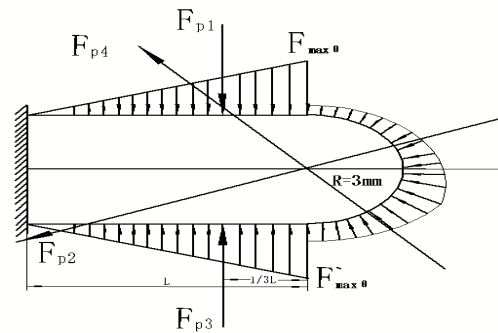


Figure A3. Cantilever beam load distribution of slide plate.

Hydraulic pressure analysis of the oil pressure chamber slider.

When the slider angle is θ .

$$F_{\max\theta} = P_{\max} \times S \quad (\text{A1})$$

where P_{\max} is the maximum pressure point on the wall of the slide in the pressure chamber, S is the unit area, $F_{\max\theta}$ denotes the maximum hydraulic pressure on the wall of the slide in the pressure chamber when the angle of rotation of the slide is θ . From the fluid simulation measurement results, it can be seen that the hydraulic pressure on the wall at the interface between the wall of the slide extension and the top profile arc is the maximum.

Length of rotor protruding from the slider: L_1

At this time, the equivalent liquid pressure at the wall of the pressure oil chamber slide

$$F_{p1} = \frac{F_{\max\theta} \cdot L_1}{2} \quad (\text{A2})$$

where F_{p1} is the equivalent fluid pressure at the wall of the pressure chamber slide.

Average hydraulic pressure in the circular part of the slider

$$q = \bar{P} \times S \quad (\text{A3})$$

where \bar{P} is the average pressure on the circular part of the slide; q indicates the average hydraulic pressure on the circular part of the slide, measured by the fluid simulation results of the root of the arc to the stator contact point. The hydraulic pressure value gradually increases, and the assumption is that the average hydraulic pressure is the load on the circular part of the slide.

The arc length of the circle is

$$L_2 = R_d \cdot \left(\frac{\pi}{2} + \alpha \right), R_d = 3 \text{ mm} \quad (\text{A4})$$

where L_2 is the length of the arc on the side of the oil pressure chamber at the contact point of the slide.

At this time, the pressure oil chamber slide arc equivalent fluid pressure

$$F_{p2} = \frac{q \cdot L_2}{2} \quad (\text{A5})$$

where F_{p2} is the equivalent hydraulic pressure of the pressure chamber slider arc.

(2) Suction chamber slider fluid pressure analysis.

When the angle of rotation of the slide is θ

$$F'_{\max\theta} = P'_{\max\theta} \times S \quad (\text{A6})$$

where P'_{\max} is the maximum pressure point on the wall of the suction chamber slide, S is the unit area, $F'_{\max\theta}$ is the maximum hydraulic pressure on the wall of the suction chamber slide when the angle of rotation of the slide is θ . The fluid simulation measurement results show that the hydraulic pressure on the wall of the slide is highest at the point where the wall of the slide extends, and the top contour arc meets.

The equivalent liquid pressure at the wall of the suction chamber slide at this time

$$F_{p3} = \frac{F'_{\max\theta} \cdot L_1}{2} \quad (\text{A7})$$

where L_1 is the length of the slide extending out of the rotor at this rotation angle; F_{p3} is the equivalent liquid pressure at the wall of the slide in the suction chamber.

The average hydraulic pressure in the circular part of the slider

$$q' = \bar{p}' \times S \quad (\text{A8})$$

where \bar{p}' is the average pressure applied to the circular part of the slide; q' is the average fluid pressure in the circular part of the slide, measured by fluid simulation, which results in the root of the arc to the stator contact point. The fluid pressure value gradually increases, and the assumption is that the average fluid pressure is the load on the circular part of the slide.

Arc length of the circle

$$L_3 = R_d \cdot \left(\frac{\pi}{2} - \alpha \right), R_d = 3 \text{ mm} \quad (\text{A9})$$

where L_3 is the length of the arc on the suction chamber side of the slide contact point.

At this time, the suction chamber slider arc equivalent liquid pressure

$$F_{p4} = \frac{q' \cdot L_3}{2} \quad (\text{A10})$$

where F_{p4} is the suction chamber slider arc equivalent pressure.

Combined with the above transition curve cavity slide different angle of the case of the hydraulic pressure on the wall of the slide pressure cavity, the hydraulic pressure on the circular surface of the slide pressure cavity, the hydraulic pressure on the wall of the slide suction cavity and the hydraulic pressure on the circular surface of the slide suction cavity are shown in Table A1.

Table A1. Equivalent stress table of alternating fluid pressure on slide plate.

θ	$F_{\max\theta}$ (kN)	F_{p1} (kN)	q (kN)	L_2 (mm)	F_{p2} (kN)	$F'_{\max\theta}$ (kN)	L_1 (mm)	F_{p3} (kN)	q' (kN)	L_3 (mm)	F_{p4} (kN)
0°	207	670.68	198	4.710	466.29	28	6.48	90.72	147	4.71	346.18
6°	260	842.4	312	5.024	783.74	96	6.48	311.04	185	4.39	406.63
12°	250	807.5	276	5.432	749.64	99	6.46	319.77	210	3.98	418.71
18°	197	602.82	175.5	6.411	562.56	118	6.12	361.08	145	3.01	218.22
24°	162	413.1	178.5	7.049	629.15	132	5.10	336.6	245	2.37	290.41
30°	187	328.18	177	7.130	631.27	169	3.51	296.59	171	2.28	195.52
36°	197	181.24	198	6.421	635.70	197	1.84	181.24	198	2.99	296.87
42°	204	54.06	188	5.453	512.59	206	0.53	54.59	199.5	1.32	131.86
48°	188	21.62	108	7.693	415.42	198	0.23	22.77	171	1.72	147.65
54°	134	33.5	112	4.720	264.34	189	0.50	47.25	103	4.69	242.02

The hydraulic pressure at the bottom of the slide has little effect on the overall force on the slide and can be abstracted as a constant value, taking the average hydraulic pressure at the bottom of the slide. According to the CFD results, the average pressure P_5 at the bottom of the slide corresponding to the transition curve cavity is 0.122 MPa, and the area S_3 at the bottom of the slide is 340.58 mm², and the hydraulic pressure F_{p5} at the bottom of the slide can be calculated according to Equation (A10) as 41,840,158.12 N.

$$F_{p5} = P_5 \times S_3 \quad (\text{A11})$$

The function approximation method was used to obtain the function of liquid pressure in the transition curve cavity. According to the results data of the liquid pressure analysis, the function fitting was carried out using Matlab's cftool toolbox to obtain the fitted function relationship equations of liquid pressure under different turning angles. The obtained function relations are shown in Equations (9)–(12) in the paper.

Appendix B

As shown in Figure A4, the contact angle between the top profile of the slide arc and the slide rotation angle. By finding the equation of the relationship between the two angles and sampling points to draw the curve, the function fitting method is applied to the curve to fit the function of the contact angle of the top profile of the slider arc and the slider rotation angle.

The equation of the polar coordinates of point A is show in Equation (A12).

$$\begin{cases} x = \rho(\theta) \cos \beta \\ y = \rho(\theta) \sin \beta \end{cases} \quad (\text{A12})$$

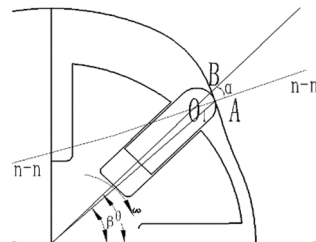


Figure A4. Stator contact angle diagram of slide piece.

Set the slope of the tangent direction at the contact point A between the transition curve of the inner cavity of the sub and the top profile of the arc as k_1 .

$$k_1 = \frac{dy}{dx} = \frac{dy}{d\beta} \cdot \frac{d\beta}{dx} = \frac{\rho'(\beta) \sin \beta + \rho(\beta) \cos \beta}{\rho'(\beta) \cos \beta - \rho(\beta) \sin \beta} \quad (\text{A13})$$

Setting the direction of the common normal at contact point A, i.e., the slope k_2 at $n - n$ in the figure, it is calculated that

$$k_2 = -\frac{1}{k_1} = \frac{\rho(\beta) \sin \beta - \rho'(\beta) \cos \beta}{\rho'(\beta) \sin \beta + \rho(\beta) \cos \beta} = f_1(\beta) \quad (\text{A14})$$

Then, the equation of the line O_1A can be expressed as

$$y - \rho(\beta) \sin \beta = f_1(\beta)(x - \rho(\beta) \cos \beta) \quad (\text{A15})$$

Let the coordinates of the center O_1 of the top profile arc of the slide be (x_1, y_1) , and since the point (x_1, y_1) is on the line O_1A , the following equation can be obtained.

$$\frac{y_1}{x_1} = \tan \theta \quad (\text{A16})$$

The collation yields Equation (A17).

$$y_1 = x_1 \cdot \tan \theta \quad (\text{A17})$$

Substituting y_1 into the equation of the line O_1A .

$$x_1 \tan \alpha - \rho(\alpha) \sin \beta = f_1(\beta)(x_1 - \rho(\beta) \cos \beta) \quad (\text{A18})$$

The collation yields Equation (A19).

$$x_1 = \frac{-f_1(\beta)\rho(\beta) \cos \beta + \rho(\beta) \sin \beta}{\tan \theta - f_1(\beta)} \quad (\text{A19})$$

Let the radius of the top profile of the blade be R_d .

$$R_d = \sqrt{(y - y_1)^2 + (x - x_1)^2} = f_3(\theta, \beta) \quad (\text{A20})$$

$R_d = 3$ mm in this design model, and the derived Equation (A21) is obtained.

$$9 = \rho^2(\beta) + \left(\sec^2(\theta) - 2\rho(\beta)(\sin \beta + \cos \beta) \right) \left[\frac{\rho(\beta) \sin \beta - \frac{\rho^2(\beta) \cos \beta \sin \beta - \rho(\beta)V(\beta) \cos^2 \beta}{V(\beta) \sin \beta + \rho(\beta) \cos \beta}}{\tan \alpha - \frac{\rho(\beta) \sin \beta - V(\beta) \cos \beta}{V(\beta) \sin \beta + \rho(\beta) \cos \beta}} \right] \quad (\text{A21})$$

Since R_d is constant, θ is a function of β . $\beta = f_4(\theta)$.

The following geometric relationship can be obtained from Figure A4.

$$\begin{cases} \sin(\theta - \beta) = \frac{|AB|}{\rho(\beta)} \\ \sin \alpha = \frac{|AB|}{R_d} \end{cases} \quad (\text{A22})$$

The collation yields Equation (A23).

$$\alpha = \sin^{-1} \left(\frac{\rho(\beta) \sin(\theta - \beta)}{3} \right) \quad (\text{A23})$$

Sampling 10 coordinate points using Matlab's cftool toolbox for function fitting, comparing multiple types of fitting approximation methods, it was found that the Gaussian approximation method was the closest to the resultant data, fitting the function relationship between the slide contact angle α and the rotation angle θ Equation (A24).

Gaussian approximation method general function model.

$$f(x) = a_1 \cdot \exp \left(-((x - b_1)/c_1)^2 \right) \quad (\text{A24})$$

The coefficient (95% confidence level) is as follows.

$$\begin{aligned} a_1 &= 48.11 & (46.15, 50.07) \\ b_1 &= 27.1 & (26.64, 27.57) \\ c_1 &= 13.89 & (13.27, 14.55) \end{aligned}$$

The result is as follows.

$$\alpha = 48.11 \cdot \exp \left(-((\theta - 27.1)/13.89)^2 \right) \quad (\text{A25})$$

References

1. Ma, W.C. Research status of high-pressure vane pump and its outlook. *Fluid Drive Control* **2006**, *6*, 1–6.
2. Liu, J.G. Development of double-acting variable vane pump. *J. Yanshan Univ.* **2002**, *3*, 276–279.
3. Jing, Y. Sliding vane pump features and development trend. *China Storage Transp.* **2008**, *12*, 116–117.
4. Huang, S.B. Innovative Design and Simulation for a Novel Vane Pump. In Proceedings of the International Conference on Mechatronics and Materials Processing, Guangzhou, China, 18–20 November 2011; pp. 354–359.
5. Karpenko, M.; Prentkovskis, O.; Šukevičius, Š. Research on high-pressure hose with repairing fitting and influence on energy parameter of the hydraulic drive. *Eksplot. I Niezawodn. Maint. Reliab.* **2022**, *24*, 25–32. [\[CrossRef\]](#)
6. Stosiak, M. Ways of reducing the impact of mechanical vibrations on hydraulic valves. *Arch. Civ. Mech. Eng.* **2015**, *15*, 392–400. [\[CrossRef\]](#)
7. Bai, J.J.; Xu, M.M. Research Status and Development Trend of Vane Pump. In Proceedings of the International Conference on Mechatronics Engineering and Computing Technology, Shanghai, China, 9–10 April 2014; pp. 1143–1146.
8. Yoshida, Y.; Tsujimoto, Y.; Kawakami, T.; Sakatani, T. Unbalance hydraulic forces caused by geometrical manufacturing deviations of centrifugal impellers. *J. Fluids Eng.* **1998**, *120*, 531. [\[CrossRef\]](#)
9. Ravindra, B.; Appasaheb, K. Prediction of flow-induced vibration due to impeller hydraulic unbalance in vertical turbine pumps using one-way fluid-structure interaction. *J. Vib. Eng. Technol.* **2019**, *8*, 417–430.
10. Li, G.P.; Chen, E.Y.; Yang, A.L.; Xie, Z.B.; Zhao, G.P. Effect of Guide Vanes on Flow and Vibroacoustic in an Axial-Flow Pump. *Math. Probl. Eng.* **2018**, *2018*, 3095890. [\[CrossRef\]](#)
11. Christopher, S.; Kumaraswamy, S. Identification of Critical Net Positive Suction Head Form Noise and Vibration in a Radial Flow Pump for Different Leading Edge Profiles of the Vane. *J. Fluids Eng. Trans. ASME* **2013**, *135*, 121301. [\[CrossRef\]](#)
12. Zhou, W.J.; Cao, Y.H.; Zhang, N.; Gao, B. A novel axial vibration model of multistage pump rotor system with dynamic force of balance disc. *J. Vib. Eng. Technol.* **2020**, *8*, 673–683. [\[CrossRef\]](#)
13. Zhang, L.J.; Wang, S.; Yin, G.J.; Guan, C.N. Fluid-structure interaction analysis of fluid pressure pulsation and structural vibration features in a vertical axial pump. *Adv. Mech. Eng.* **2019**, *11*, 1687814019828585. [\[CrossRef\]](#)
14. Liu, H.L.; Cheng, Z.M.; Ge, Z.P. Collaborative improvement of efficiency and noise of bionic bane centrifugal pump based on multi-objective optimization. *Adv. Mech. Eng.* **2021**, *13*, 1687814021994976. [\[CrossRef\]](#)
15. Si, Q.R.; Wang, B.B.; Yuan, J.P. Numerical and Experimental Investigation on Radiated Noise Characteristics of the Multistage Centrifugal Pump. *Processes* **2019**, *7*, 793. [\[CrossRef\]](#)
16. Cheng, Y.Q.; Wang, X.H.; Chai, H. The Theoretical Performance Analysis and Numerical Simulation of the Cylindrical Vane Pump. *Arab. J. Sci. Eng.* **2021**, *46*, 2947–2961. [\[CrossRef\]](#)
17. Liu, L.; Ding, C.; Wang, P.F. Design and Optimization of the Transition Curve in the Novel Profiled Chamber Metering Pump. *J. Multi-Body Dyn.* **2020**, *234*, 435–446. [\[CrossRef\]](#)
18. Fan, J.; Wang, Z.R. Calculation and analysis of single-acting vane pump stator radial fluid pressure for high-powered remote water supply fire truck water collection system. *Fire Technol. Prod. Inf.* **2013**, *11*, 47–50.
19. Cho, I.S. Behavioral characteristics of the vane of a hydraulic vane pump for power steering systems. *J. Mech. Sci. Technol.* **2015**, *29*, 4483–4489. [\[CrossRef\]](#)
20. Lei, H.; Hu, H.J.; Lu, Y. A dynamic analysis on the transition curve of profiled chamber metering pump. *J. Dyn. Syst. Meas. Control* **2016**, *138*, 071003. [\[CrossRef\]](#)
21. Gao, P. Application of Matlab's Cftool toolbox to flotation tailings ash and image grayness curve fitting. *Coal Process. Technol.* **2015**, *1*, 67–70.
22. Hou, Z.R.; Lu, Z.S. MATLAB-based particle swarm optimization algorithm and its application. *Comput. Simul.* **2003**, *10*, 68–70.
23. Wang, L.J.; Jiang, S.F.; Xu, F.X. Analysis of particle swarm algorithms and their covariates. *J. Qiqihar Univ.* **2019**, *35*, 14–17.